

Cell Surface Electrochemical Heterogeneity of the Fe(III)-Reducing Bacteria *Shewanella putrefaciens*

I. SOKOLOV,[†] D. S. SMITH,[†]
G. S. HENDERSON,[†] Y. A. GORBY,[‡] AND
F. G. FERRIS*[†]

Department of Geology, University of Toronto,
22 Russell Street, Toronto, Ontario, M5S 3B1 Canada, and
Pacific Northwest National Laboratories, P.O. Box 999,
MS P7-50, Richland, Washington 99352

Acid–base titration experiments and electrostatic force microscopy (EFM) were used to investigate the cell surface electrochemical heterogeneity of the Fe(III)-reducing bacteria, *Shewanella putrefaciens*. The acid–base titrations extended from pH 4 to 10, and the titration data were fit using a linear programming pK_a spectrum approach. Overall, a five-site model accounted for the observed titration behavior with the most acidic sites corresponding to carboxylic groups and phosphodiester groups, intermediate sites phosphoryl groups, and two basic sites equivalent to amine or hydroxyl groups. The pH for the point of zero charge on the bacteria was 5.4. In EFM images of cells rinsed in solutions at pH 4.0, 7.0, and 8.0, a pronounced increase in small (≤ 100 nm diameter) high contrast patches was observed on the cells with increasing pH. The pH dependence of EFM image contrast paralleled the pattern of cell surface charge development inferred from the titration experiments; however, quantitative analysis of high contrast regions in the EFM images yielded lower surface charge values than those anticipated from the titration data. For example at pH 7, the calculated surface charge of high contrast regions in EFM images of the bacterial cells was $-0.23 \mu\text{C}/\text{cm}^2$ versus $-20.0 \mu\text{C}/\text{cm}^2$ based on the titration curve. The differences in surface charge estimates between the EFM images and titration data are consistent not only with charge development throughout the entire volume of the bacterial cell wall (i.e., in association with functional groups that are not directly exposed at the cell surface) but also with the presence of a thin structural layer of water containing charge-compensating counterions. In combination, the pK_a spectra and EFM data demonstrate that a particularly high degree of electrochemical heterogeneity exists within the cell wall and at the cell surface of *S. putrefaciens*.

Introduction

Dissimilatory iron-reducing bacteria (DIRB) couple the oxidation of reduced organic matter or hydrogen to the

reduction of Fe(III) as a mode of energy-yielding respiration (1). These bacteria are the most important and metabolically active members of microbial communities in anaerobic, nonsulfidogenic environments, where they extensively promote valence transitions of iron from Fe(III) to Fe(II) (2, 3). Results from early studies suggested that DIRB could reduce only poorly crystalline hydrous ferric oxides (HFO) (1, 4); however, knowledge of the types of Fe(III)-bearing minerals that can serve as electron acceptors for these microorganisms and the factors that control the rate and extent of their reduction has expanded greatly. Recent evidence indicates that DIRB can in fact reduce crystalline phases of iron oxide, such as goethite, hematite, and magnetite, that are common components of subsurface sediments (5–7) as well as structural Fe(III) in smectite clays (8, 9). A variety of additional factors, including pH, oxide surface area, and post-reduction bacteriogenic Fe(II) concentrations, also appear to exert some control on the rate and extent of reduction of these minerals (6, 10–12).

The Fe(II) produced as a consequence of DIRB activity may partition into the aqueous phase, sorb to solid surfaces, including the DIRB themselves, or, depending on the geochemical conditions, become incorporated into various secondary reduced iron-bearing mineral phases. For example, magnetite (Fe_3O_4), siderite (FeCO_3), and vivianite ($\text{Fe}(\text{PO}_4)_2 \cdot (8\text{H}_2\text{O})$) are frequently observed as products of dissimilatory Fe(III) reduction (13–15). The ability of DIRB to promote the precipitation of reduced-iron minerals is impacted not only by the extent to which substrate iron oxides undergo reductive dissolution but also by cellular sorption of Fe(II) and other constituent ions or molecules of the mineral (6, 10, 12). This later process, which can be attributed to the presence of reactive acidic groups (e.g., carboxyl and phosphoryl) in cell wall and capsular polymers, lowers the interfacial surface energy of nascent crystal nuclei and catalyzes mineral precipitation by reducing the activation energy barrier to the nucleation process (16–18). In addition, some Fe(II)-bearing minerals produced by DIRB can incorporate polyvalent metal cations into their crystal lattice (19, 20). Consequently, formation of Fe(II)-bearing minerals may control the fate and transport of these contaminants in subsurface environments where DIRB are active.

Although DIRB play an important role in regulating the aqueous geochemistry of iron and other metals, little work has directly assessed the cell surface electrochemistry of DIRB or the nature of the interfacial environment around individual cells. The electrochemical properties of particulate solids are often inferred from titrations in which net surface charge is determined, assuming electroneutrality, as the difference between known added amounts of acid and base and measured proton concentration. The resultant titration curve can then be fit to a speciation model for the system to determine pK_a values and site densities of reactive surface sites. This approach has recently been used to assess functional group heterogeneity on bacterial surfaces (18). Moreover, with the development of noncontact electrostatic force microscopy (EFM), it is now possible to directly inspect and quantify charge development on surfaces (21–23). In this paper, a combination of acid–base titrations and EFM are applied to assess the electrochemical surface properties of the groundwater DIRB, *Shewanella putrefaciens*.

Experimental Section

Growth of Bacteria. *Shewanella putrefaciens* strain CN-32, a facultative Fe(III)-reducing bacteria, was used as the primary test organism for the investigation. This organism was isolated

* Corresponding author phone: (416)978-0526; fax: (416)978-3938; e-mail: ferris@quartz.geology.utoronto.ca.

[†] University of Toronto.

[‡] Pacific Northwest National Laboratories.

from an anaerobic aquifer in northwestern New Mexico and has been deposited in the Subsurface Microbial Culture Collection located at the Oregon Graduate Institute (D. Boone, SMCC Curator). For experimental work, Strain CN-32 was grown for 15–16 h in aerobic shake cultures at 30 °C using Tryptic Soy Broth (TSB) as a complete growth medium. Cells were recovered from the growth medium by sterile transfer to acid-washed, autoclaved bottles, and centrifuged at 7000 rpm for 10 min.

Preparation of Cells for Titration. The broth was decanted from centrifuged cultures, and the cells were resuspended in sterile 18 MΩ water. After further centrifugation, the cells were resuspended in 0.1 M KNO₃ prepared in sterile 18 MΩ water and soaked for 30 min before centrifuging. This was followed by three rinses with 0.1 M KNO₃ solution, and finally the cells were resuspended in a sterile solution of 0.1 M KNO₃. Inspection of the bacteria using the BacLight fluorescent viability stain (Molecular Probes) confirmed that this washing procedure did not adversely affect cell viability (18).

Solutions. All solutions for the titration experiments were degassed for 20 min with 99.998% N₂ and kept in an anaerobic chamber when not in use to keep out O₂ and particularly CO₂, which would affect the pH. The solutions and titration aliquots (i.e., background electrolyte solution and bacterial suspension) were also degassed again immediately prior to titration and kept under a positive pressure of N₂.

The 0.1 M NaOH titrant solution was prepared using degassed water in an anaerobic chamber from standard 10 M NaOH solution (ACP Chemicals Inc.). The sodium hydroxide titrant solution was standardized by titration against a known weight of dried potassium hydrogen phthalate (Fisher ACS grade). The 0.1 M HCl titrant solution was prepared by dilution of 10 M standard HCl (ACP Chemicals Inc.) in sterile 18 MΩ water. The exact concentration of HCl titrant solution was determined by titration against the standardized NaOH solution.

Titration. All titrations were performed in a closed glass vessel under positive pressure of N₂ and mixed using a Teflon magnetic stir bar. The titrations were controlled by a Metrohm GP 736 Titrimo unit interfaced by Titrimo Workcell v3.1 software to a personal computer. A buret exchange unit with a 20 mL buret was employed for NaOH. A known volume of HCl was added at the beginning of the titration to lower the pH to around 3. Temperature was fixed at 25.0 °C by performing the titrations inside an incubator (VWR model 2005). The pH electrode (Ross SurFlow) was calibrated directly into concentration units using blank titrations (0.1 M KNO₃) following the method used by Masini et al. (24) to obtain junction potential correction factors. In addition, blank titrations serve as an excellent test for CO₂ contamination in that more than one endpoint will be observed if contamination has occurred. In our blank titrations only one endpoint was ever found, demonstrating that CO₂ contamination is negligible in our experimental system.

The optical density at 600 nm (OD₆₀₀) of the washed bacterial suspensions were measured using a Milton Roy Spectronic spectrophotometer prior to each titration run. The measured OD₆₀₀ was compared to a prepared calibration curve to determine the dry weight concentration of bacteria (mg/L). The bacteria concentrations were approximately 400 mg/L for each titration. A known volume of the bacterial suspension, typically 50 mL, was then transferred to the titration vessel, which was immediately connected to the N₂ gas line. The pH of the bacterial suspension was then adjusted to a value around 3.0 and was allowed to equilibrate for 30 min before titration with NaOH up to a pH near 10.0.

Using the Titrimo Workcell software the titration method allowed for variable additions of titrant to keep approximately equal pH intervals. After each addition of titrant the potential

was followed until the change was less than 0.1 mV/min, and then the next aliquot of titrant was added.

Analysis of Titration Data. The titration data were analyzed using the linear programming – pK_a spectrum method (LPM), as described by Brassard et al. (25) and applied to bacteria surfaces by Cox et al. (18). The titration data are expressed in the form charge excess versus –log[H⁺]. Where charge excess (*b*) is calculated as $b = C_b - C_a + [H^+] - K_w/[H^+]$ for the known concentrations of acid (*C_a*) and base (*C_b*) added as well as the measured proton concentration and stability constant for the disassociation of water (*K_w*). To determine pK_a values and site densities for binding sites on the bacteria surface it is necessary to model *b*, the charge excess due to deprotonation of sorption sites. Here the surface sites are considered as a sum of *n* monoprotic ligands (L[–]) with dissociation constants *K_{ai}* and concentrations *L_{Ti}*. For the *j*th addition of titrant

$$b_j = \sum_{i=1}^n [L^-]_i + S = \sum_{i=1}^n \left(\frac{K_{a_i} L_{T_i}}{K_{a_i} + [H^+]_j} \right) + S \quad (1)$$

where *S* is a constant term analogous to the acid neutralizing capacity (ANC) as in Brassard et al. (25) or the initial protonation state of the surface (26). In practice *S* allows for modeling positive charge on the surface because representing the titration curve as a sum of monoprotic sites can only account for negative charges using the [L[–]] terms.

To determine the best-fit *K_i/L_{Ti}* pairs the pK_a spectrum approach is used here. In this approach the pK_a = –log(*K_{ai}*) values are fixed in a constant sequence going from a minimum value to a maximum value at fixed step sizes. For the data here the minimum and maximum pK_a values correspond to the minimum and maximum measured pH, respectively, and the step size is fixed at 0.2. What remains is to solve for the *L_{Ti}* value associated with each pK_{ai} and to solve for the *S* term. In practice this minimizes the number of sites because most *K* values are assigned a ligand concentration of zero, and *S* converges on a constant value. The details of the linear programming method to solve this problem are given by Brassard et al. (25). It should be noted that the constants reported here are conditional on ionic strength (0.1 M KNO₃), and no effort has been made to correct for electrostatic effects. The constant ionic strength was utilized to ensure that ionic activity coefficients should remain constant over the course of the titration; thus the determined constants are conditional on ionic strength. The assignment of the peaks in the pK_a spectrum to possible types of reactive surface groups is operational but does give some idea of the types of surface groups that are likely to exist on the bacteria surface.

Atomic and Electrostatic Force Microscopy. Aliquots of the washed bacterial cell suspensions were adjusted to pH 4, 7, and 8 using HCl or NaOH solutions. After soaking for 30 min, small droplets of the bacterial suspensions were placed on cleaved sections of mica that were premounted on a standard AFM mount by means of epoxy glue. The droplets were left undisturbed for about 5 min, and then excess solution was removed with a piece of filter paper. A drop of pH-adjusted water was subsequently flushed over the mica surface to remove loosely attached bacteria. Excess water was again taken-up with filter paper to ensure that the bacteria were not displaced from the mica during scanning. The samples were then left to dry for 5 min under ambient conditions before being placed onto the AFM stage.

All atomic and electrostatic force microscopy images were obtained using a Digital Instruments NanoScope IIIa equipped with a phase extender module and operating in EFM-mode. The *A+B* feedback signal was about 3 V, while the RMS signal was set at around 1.5 V. Feedback main scan

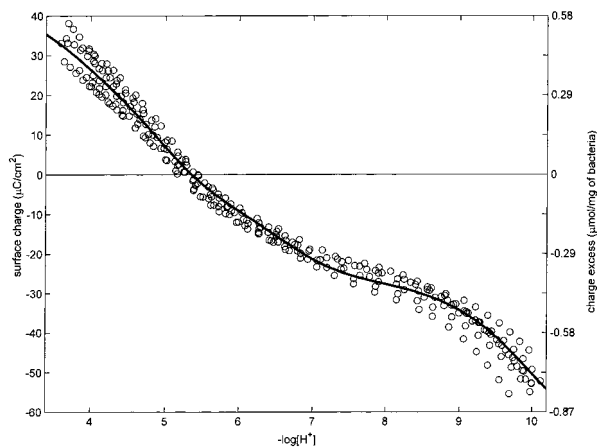


FIGURE 1. Acid–base titration curves for eight replicate titrations of *Shewanella putrefaciens* strain CN-32.

gain parameters were set between 1 and 2 for both integral and proportional gains. Force modulation gains for interleave scanning were set between 150 and 300 for both integral and proportional gains. A Digital Instruments Nanoprobe MESP metal-coated tip (cantilever length 224 μm , resonance frequency 54–105 kHz, spring constant $k \sim 1.2\text{--}2.7$ N/m) and the D scan head (maximum scan area is 12.5×12.5 μm^2 , z-sensitivity is 9 nm/V) were employed throughout the study. Scan rates were chosen from 0.5 to 1.5 Hz with contact AFM being performed on each primary trace and noncontact EFM on each secondary retrace at a distance of 10 nm above the specimen surface.

Results and Discussion

The data from eight replicate acid–base titrations of *S. putrefaciens* strain CN-32 is shown in Figure 1. The measured ligand charge balance (i.e., $\mu\text{mol/mg}$ dry weight of bacteria) has been transformed to surface charge ($\mu\text{C/cm}^2$) by assuming a surface area of 140 m^2/g for the bacteria, as estimated by Fein et al. (27). Figure 2(a–h) shows each of the associated $\text{p}K_a$ spectra determined by LPM for the eight titrations. The mean value and one standard deviation of S from all eight determinations is 0.62 ± 0.16 $\mu\text{mol/mg}$ of bacteria. Figure 2(i) is a composite overlay of all of the $\text{p}K_a$ spectra. The replicate titrations exhibit some variation in terms of number of sites and $\text{p}K_a/L_T$ values, but the overlay spectrum clearly shows distinct clusters of $\text{p}K_a$ values. To summarize these data, five ranges of $\text{p}K_a$ values were determined by inspection and assigned to five different classes of ligands (Table 1). In selecting the number of ligand classes and their $\text{p}K_a$ ranges, the criteria was not a minimum number of sites to describe the data but rather a minimum number of sites containing all the variations in $\text{p}K_a$ values.

For each ligand class a mean $\text{p}K_a$ value was determined by using a weighted mean calculation, where the weighting factors are the corresponding ligand concentrations. A proposed confidence region about this estimate was calculated using a weighted standard deviation calculation, as Cox et al. (18). In addition, regular mean and standard deviation calculations were performed on the total ligand concentrations in each group of $\text{p}K_a$ values. This approach to summarize multiple $\text{p}K_a$ spectra as a generalized five-site model was also used by Cox et al. (18). The five-site model for *S. putrefaciens* strain CN32 is summarized in Table 1. This synopsis of the $\text{p}K_a$ spectra allows for comparison to other published results which are generally reported as discrete individual sites (27). When the charge is calculated using this proposed five-site model, the solid line in Figure 1 is obtained which agrees very well with the experimental data.

In all EFM images, the change in frequency contrast is shown with a maximum scale of 20 Hz. Dark areas correspond to the presence of a strong force gradient and bright areas to a weak force gradient. Results for pH conditions of 4.0, 7.0, and 8.0 are shown in Figures 3–5, respectively. Parts a and b of Figure 3 compare the AFM and noncontact EFM images of the bacterial surface for the case of pH 4.0. The rod-shaped morphology of *S. putrefaciens* is obvious in the AFM image (Figure 3a), whereas there is no distinguishing frequency contrast associated with the cell in the corresponding EFM image (Figure 3b). It should be noted that our discussion of AFM images are actually deflection channel images, which are proportional to the actual topography. AFM and EFM images for the case of pH 7.0 are shown in Figure 4. At the higher pH, a pronounced increase in frequency contrast was observed, revealing cell shape in the EFM image (Figure 4b). On a smaller scale, a heterogeneous distribution of high contrast patches, approximately 100 nm in diameter and less, characterize the cell surface (Figure 4c). The EFM image contrast becomes even more pronounced at pH 8.0 (Figure 5). This progressive increase in frequency contrast observed in the EFM images of *S. putrefaciens* with increasing pH closely parallels the pattern of surface charge development revealed by the titration experiments (Figure 1). At the same time, the AFM images (Figures 3a, 4a, and 5a) reveal an increase in cell surface roughness.

The cell surface charge density associated with the frequency contrast in the EFM images can be estimated in accordance with the following assumptions. First, a homogeneous distribution of charge is present within any small flat disk of radius R . Second, an induced charge develops on the conductive AFM tip that can be set as a point charge. The assumption that the tip can be represented as a point charge is approximately valid for the metal coated tips that we used in this study. The electrical force gradient acting between such a charged disk and the point charge on the AFM tip is thus given by (28, 29)

$$F = -\frac{q\bar{\sigma}}{2\epsilon_0} \frac{R^2}{(R^2 + d^2)^{3/2}} \quad (2)$$

where d is the distance between the charge on the tip and the disk, q is the induced charge on the tip, and $\bar{\sigma}$ is the surface charge density of the disk as detected by the AFM tip. In addition, the force gradient can be written as

$$F = 2k \frac{\Delta f}{f} \quad (3)$$

where k is the cantilever spring constant, Δf is the measured frequency shift, and f is the resonant frequency of the cantilever. Combining eqs 2 and 3 together yields

$$\bar{\sigma} = -\frac{4\epsilon_0 k (R^2 + d^2)^{3/2}}{q} \frac{\Delta f}{R^2 f} \quad (4)$$

The induced charge q is equal to the total charge of the disk (i.e., $\pi \bar{\sigma} R^2$). This is practical because the nonconductive bacterial cell surface is removed some distance from the tip (i.e., 10 nm in the case of this study), and consequently there is no contribution from an induced charge on the cell. Taking into account eqs 2–4, one finally has

$$\bar{\sigma} = \sqrt{-\frac{4\epsilon_0 k (R^2 + d^2)^{3/2}}{q} \frac{\Delta f}{R^4 f}} \quad (5)$$

To estimate the surface charge the values of the parameters are set as follows: $k = 2.0$ N/m, $f = 50$ kHz, and $d = 10$ nm. Considering the size of high contrast regions in Figures 4c

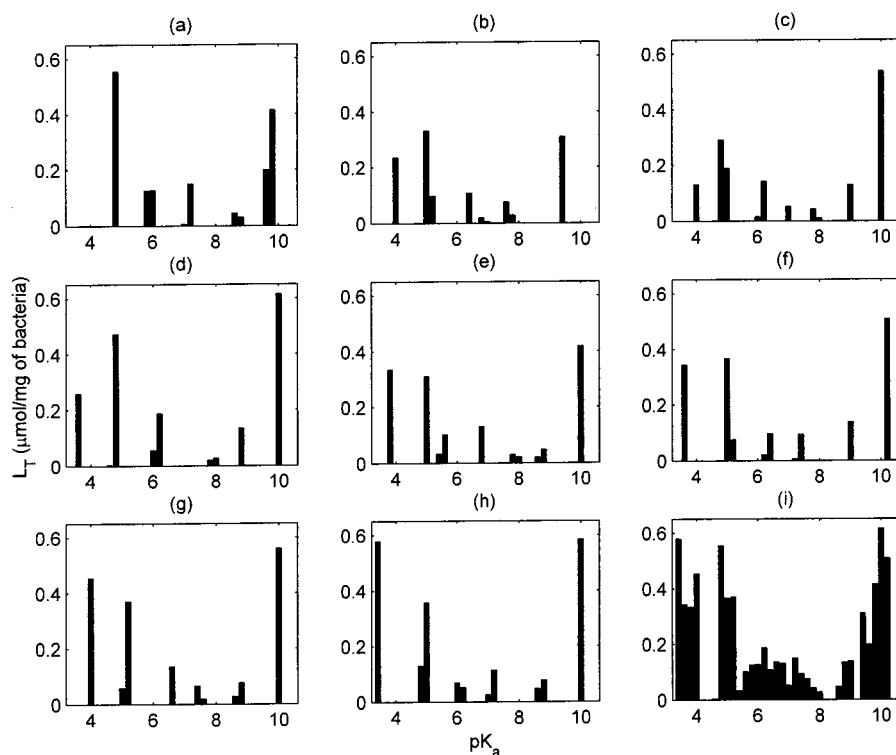


FIGURE 2. (a)–(h) pK_a spectra determined by linear programming analysis for each of the eight titration curves shown in Figure 1. An overlay plot of all eight pK_a spectra is given in (i).

TABLE 1. Summary of pK_a Values for a Five-Site Model Obtained from Analysis of the *Shewanella putrefaciens* Titration Data by Linear Programming

ligand class	range of pK_a values	pK_a value ^a	L_T value (μmol/mg) ^a	functional group ^b
1	3.4–4.0	3.72 ± 0.06	0.29 ± 0.18	phosphodiester
2	4.6–5.4	4.95 ± 0.02	0.45 ± 0.07	carboxylic/phosphoryl pK_1
3	5.6–8.0	6.64 ± 0.50	0.28 ± 0.06	phosphoryl pK_2
4	8.6–9.0	8.83 ± 0.02	0.10 ± 0.05	amine
5	9.4–10.2	9.99 ± 0.01	0.65 ± 0.36	amine/hydroxyl

^a Confidence intervals are given as one standard deviation. ^b As proposed by Cox et al. (18).

and 5c, a maximum value of $R = 10.0$ nm is assumed to satisfy the conditional assumption of homogeneous charge distribution. In the discussion leading to the development of eq 5 we have omitted the meniscus of water between the sample and the tip and the water retained by the bacteria during sample preparation. These aspects and their possible influence on the charge estimates by EFM are discussed further below.

For a high contrast region on the *S. putrefaciens* cell surface at pH 7.0 (Figure 4c), $\Delta f = 42$ Hz. Equation 5 yields a value for $\bar{\sigma} \sim -0.23 \mu\text{C}/\text{cm}^2$. Similarly, at pH 8.0 (Figure 5c) $\Delta f = 56$ Hz and $\bar{\sigma} \sim -0.27 \mu\text{C}/\text{cm}^2$. This suggests that the surface charge in high contrast regions at pH 8.0 is about 13% higher than in high contrast regions at pH 7.0. These results compare favorably with those from the titration experiments where estimated surface charge at pH 8.0 was found to be approximately 22% greater than at pH 7.0 (Figure 1). At the same time, however, the patchy distribution of high contrast charged areas in the EFM images implies not only that little or no surface charge exists over wide areas of the *S. putrefaciens* cell surface but also that much of the electrostatic charge anticipated from the titration experiments is deep in the cell wall and inaccessible to interrogation by noncontact EFM. In addition, if the sample surface was not completely

dry and a meniscus of water formed between the tip and the sample, the EFM charge estimates would underestimate the actual charge.

The development of surface charge on *S. putrefaciens* strain with increasing pH agrees qualitatively with the pH dependent charging reported by Plette et al. (30) for isolated cell walls from *Rhodococcus erythropolis*. In particular, the pH for the zero point of charge on *S. putrefaciens* is around 5.4, compared with about 5.6 for the *R. erythropolis* cell walls. The charging behavior for *S. putrefaciens* strain reported here is also similar in magnitude to that reported for hydrous ferric oxide and other mineral surfaces. For example, hydrous ferric oxide at 0.1 M ionic strength is reported to have a surface charge of $30 \mu\text{C}/\text{cm}^2$ at pH 4 (31), while our calculated charge for *S. putrefaciens* is between 29 and $38 \mu\text{C}/\text{cm}^2$ at pH 4.

To describe the proton binding of isolated *R. erythropolis* cell walls, Plette et al. (30) proposed a three-site complexation model with the most acidic sites attributed to carboxylic sites ($pK_a = 4.62$, $L_T = 0.503 \mu\text{mol}/\text{mg}$ of cell wall), intermediate sites corresponding to phosphoryl sites ($pK_a = 7.83$, $L_T = 0.193 \mu\text{mol}/\text{mg}$ of cell wall), and the highest pK_a sites attributed to amine sites ($pK_a = 9.96$, $L_T = 0.235 \mu\text{mol}/\text{mg}$ of cell wall). While these three sites are within a pK_a unit of three of the five sites proposed here for *S. putrefaciens*, the five-site model has an additional acidic site and an additional intermediate pK_a site. In addition, the site concentrations are within 20% except, the most basic *S. putrefaciens* sites have about three times higher concentration than was determined for the *R. erythropolis* cell walls alone. These variations in site concentrations are very likely related to differences in the macromolecular composition of the *R. erythropolis* and *S. putrefaciens* cell walls (18, 30).

In another study, Cox et al. (18) applied linear programming to identify five classes of ligand sites in pK_a spectra from titrations of intact *Bacillus subtilis* cells at an ionic strength of 0.1 M KNO_3 . The most acidic site has a $pK_a = 5.2$ which is much less acidic than the most acidic site proposed here

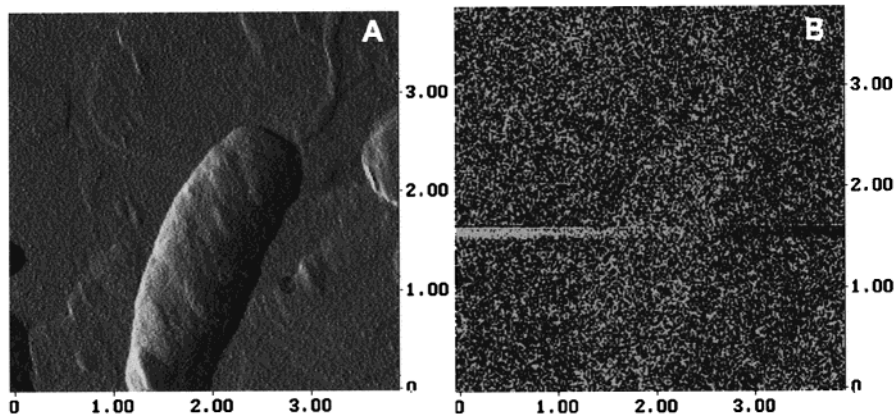


FIGURE 3. (A) Atomic force microscopy topographic image of a $4.0 \times 4.0 \mu\text{m}^2$ area showing a *Shewanella putrefaciens* cell from a pH 4 rinse. (B) Electrostatic force microscopy image of the same area showing the weak contrast associated with the bacterial cell.

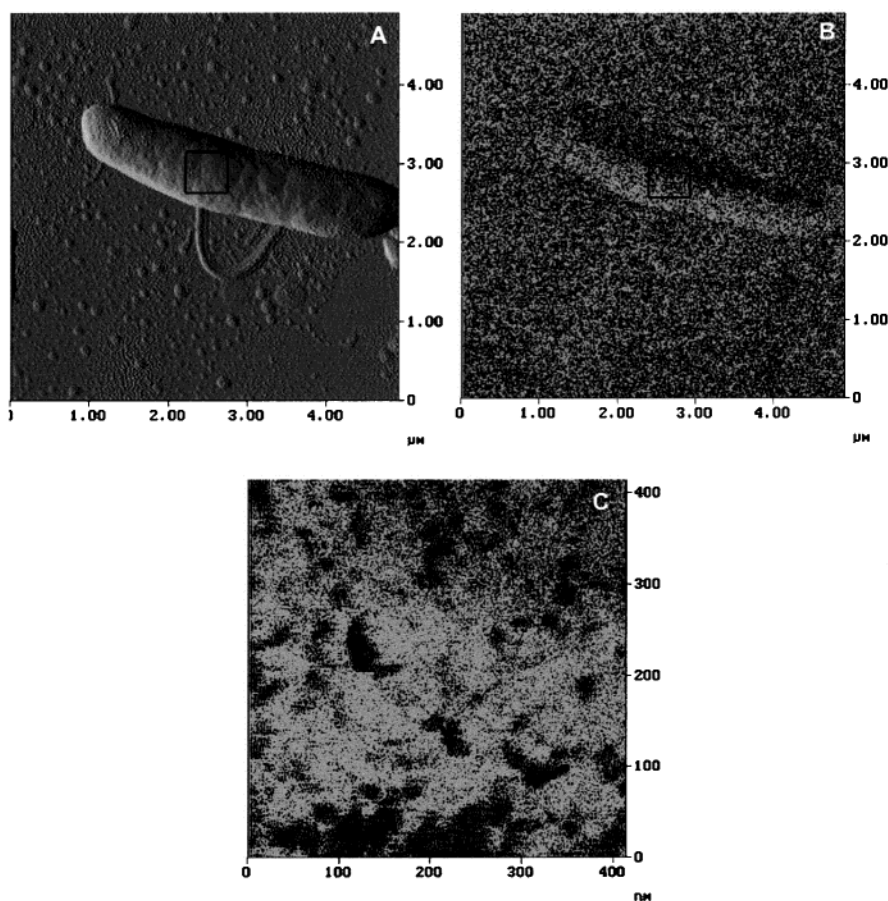


FIGURE 4. (A) Atomic force and (B) electrostatic force microscopy images of the same $5.0 \times 5.0 \mu\text{m}^2$ area showing a *Shewanella putrefaciens* cell from a pH 7.0 rinse. (C) An electrostatic force microscopy image of the $420 \times 420 \text{ nm}^2$ area indicated on the surface of the bacterial cell shown in A and B.

at a pK_a value of 3.72. Other than that, the pK_a values for the five ligand classes among the two bacteria are similar within a pK_a unit of each other. The site densities for *S. putrefaciens* are higher than those determined for *B. subtilis* though. The total site density for *Bacillus subtilis* was determined to be $0.5 \mu\text{mol}/\text{mg}$ of bacteria (18), but here our value for *S. putrefaciens* is about 3 times higher at $1.77 \mu\text{mol}/\text{mg}$ of bacteria. In particular, the site densities at the intermediate pK_a values for *S. putrefaciens* strain are higher than for *B. subtilis*, as might be anticipated for the presence of phosphoryl groups in lipopolysaccharide (LPS) of the outer membrane (32). Overall, the types of functional groups corresponding to the proposed sites are likely carboxylic and

phosphodiester sites for the two most acidic sites, phosphoryl sites for the intermediate pK_a value, and amine or hydroxyl sites for the two highest pK_a sites (Table 1). A complete discussion of types of functional groups on bacteria surfaces is given by Cox et al. (18).

The observed contrast in the *S. putrefaciens* noncontact EFM images is consistent with long-range electrostatic force interactions between charged regions on the bacterial cell surface and the AFM tip (28, 29, 33). This premise is strengthened considerably by both the pH dependence of image contrast, increasing markedly from pH 4.0 to 8.0, and the documented charging behavior of the bacteria witnessed in the titration experiments. Considering the five classes of

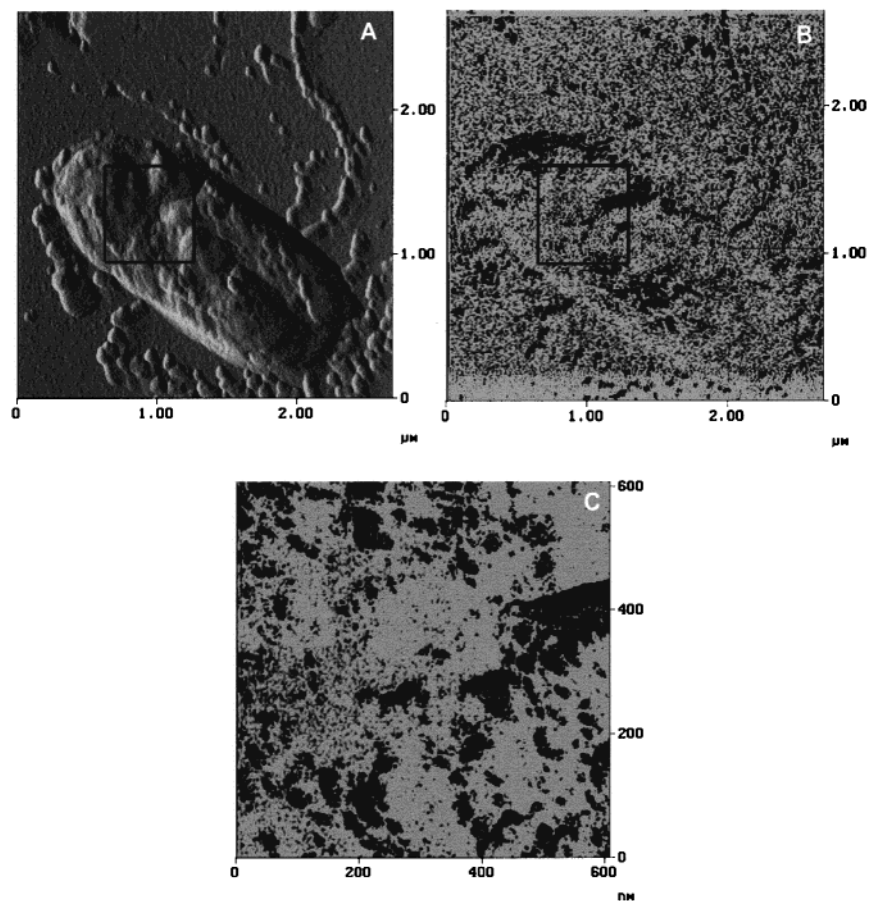


FIGURE 5. (A) Atomic force and (B) electrostatic force microscopy images of the same $2.7 \times 2.7 \mu\text{m}^2$ area showing a *Shewanella putrefaciens* cell from a pH 8.0 rinse. (C) An electrostatic force microscopy image of the $610 \times 610 \text{ nm}^2$ area indicated on the surface of the bacterial cell shown in A and B.

ligand sites identified in the *S. putrefaciens* pK_a spectra, the high contrast observed in EFM images for pH 7.0 and 8.0 fall within the range anticipated for deprotonation of phosphoryl groups with an intermediate pK_a value (18, 27). Conversely, the poor contrast observed at pH 4.0 corresponds to the most acidic of the five ligand classes and a condition where the majority of the other sites remain protonated, notably amine groups which are capable of imparting a net positive surface charge to the bacterial cells.

Because the outer membrane of Gram-negative bacteria like *S. putrefaciens* is assembled in a highly asymmetric fashion, LPS exists as the major structural macromolecule that is exposed on the exterior surface (32, 34). The presence of both carboxyl and phosphoryl groups in LPS, coupled with the exposure of these groups at the surface of the outer membrane and their deprotonation over a pH range of 5.0–8.0, provides a good explanation for the development of contrast in higher pH condition EFM images. In the same way, amine groups occur in proteins embedded within the outer membrane as well as in the underlying peptidoglycan layer (34, 35). As such, these groups would be effectively screened from EFM scanning and, as observed, yield little or no contrast at pH 4.0 in a fully protonated state.

The islands of high contrast that distinguish the EFM images at the pH 7.0 and 8.0 conditions indicate that the exposed surface charge on *S. putrefaciens* is characterized by a rather heterogeneous spatial distribution. At least some of the high contrast patches seem to be associated with raised surface structures, particularly at pH 8.0 where a pronounced increase in cell surface roughness was observed. In terms of appearance, these raised structures resemble blisters or blebs that develop commonly on the outer membrane of other

Gram-negative bacteria (34, 36). The formation of such blebs is exacerbated greatly by exposure of cells to metal chelators such as EDTA and is interpreted to be caused by an increase in electrostatic repulsion between adjacent charged molecules (32, 34, 37). This insight on bleb formation provides a reasonable explanation for the increased surface roughness and EFM contrast observed at pH 7.0 and 8.0 with *S. putrefaciens*.

The surface charge estimated from the EFM images (i.e., $-0.23 \mu\text{C}/\text{cm}^2$ to $-0.27 \mu\text{C}/\text{cm}^2$ at pH 7.0 and 8.0, respectively) was considerably lower than the $20\text{--}30 \mu\text{C}/\text{cm}^2$ anticipated from the titration experiments. There are two main reasons that account for this difference. First, charge development occurs throughout the entire volume of the cell wall in association with macromolecular components that are not directly exposed at the cell surface, such as the peptidoglycan layer (34, 35). Second, the fixed surface charge on any particulate solid in suspension must normally be fully compensated by diffuse layer counterions over a distance greater than, or equal to, the interfacial Debye length (k^{-1}) to satisfy the requirement for electroneutrality of the interfacial system as a whole (31, 38). Estimates for k^{-1} are usually on the order of several nanometers for natural particulate solids with surface charges similar to those obtained for *S. putrefaciens* (39). Even after the removal of excess water, individual bacterial cells are likely to retain a structural layer of water at least as thick as k^{-1} that contains surface charge-compensating counterions. Consequently, the net surface charge detected by EFM at a distance from the surface that approaches k^{-1} (i.e., 10 nm in this investigation) will be reduced somewhat relative to the actual surface charge because of the presence of intervening counterions. In

addition, the two charge estimate methods prepare the samples in a different way. For EFM the bacteria are attached to a solid substrate and for titration experiments the bacteria are in solution; it is possible that charging of the bacteria surface is dependent on whether the bacteria is bound to some substrate. The discussion here assumes that bacterial sorption to a surface does not significantly affect the charging of the cell surface compared to how it would behave completely suspended in solution.

The pK_a spectra and EFM data show together that a high degree of electrochemical heterogeneity exists within the cell wall and at the cell surface of *S. putrefaciens*. Recognition of variations in the nature and spatial distribution of reactive sites that contribute to charge development on these bacteria implies further that the cell surface of these Fe(III)-reducing bacteria functions as a highly differentiated interfacial system capable of supporting multiple intermolecular interactions with both solutes and solids. These include surface complexation reactions involving dissolved metals as well as adherence to mineral substrates such as hydrous ferric oxide through longer-range electrostatic interactions and surface precipitation of secondary reduced-iron minerals.

These experiments comprise a first effort in trying to assess bacterial cell surface electrochemical heterogeneity using a comparative multiple response approach. The results are consistent with the known structure and chemistry of bacterial cell walls and provide a more fully integrated basis for understanding some of the processes that occur at bacterial cell surfaces. Moreover, future studies employing EFM measurements to examine bacterial–mineral interactions directly in aqueous solutions promise to yield significant new insight on the reactive interfacial chemistry of biomineral composites.

Acknowledgments

This work was supported in full by Grant no. DE-FG02-99ER627351, Natural and Accelerated Bioremediation Research (NABIR) program, Office of Biological and Environmental Research, United States Department of Energy.

Literature Cited

- (1) Lovley, D. R. *Microbiol. Rev.* **1991**, *55*, 259.
- (2) Lovley, D. R. *FEMS Microbiol. Rev.* **1997**, *20*, 305.
- (3) Lovley, D. R.; Chapel, F. H. *Rev. Geophysics.* **1995**, *33*, 365.
- (4) Lovley, D. R.; Phillips, E. J. P. *Appl. Environ. Microbiol.* **1988**, *54*, 1472.
- (5) Zachara, J. M.; Frederickson, J. K.; Li, S. M.; Kennedy, D. W.; Smith, S. C.; Gassman, P. L. *Am. Mineral.* **1998**, *83*, 1426.
- (6) Urrutia, M. M.; Roden, E. E.; Zachara, J. M. *Environ. Sci. Technol.* **1999**, *33*, 4022.
- (7) Roden, E. E.; Urrutia, M. M.; Mann, C. J. *Appl. Environ. Microbiol.* **2000**, *66*, 1062.
- (8) Kostka, J. E.; Stucki, J. W.; Nealson, K. H.; Wu, J. *Clays Clay Miner.* **1996**, *44*, 522.
- (9) Kostka, J. E.; Wu, J.; Nealson, K. H.; Stucki, J. W. *Geochim. Cosmochim. Acta* **1999**, *63*, 3705.
- (10) Roden, E. E.; Urrutia, M. M. *Environ. Sci. Technol.* **1999**, *33*, 1847.
- (11) Urrutia, M. M.; Roden, E. E.; Frederickson, J. K.; Zachara, J. M. *Geomicrobiol. J.* **1998**, *15*, 269.
- (12) Roden, E. E.; Zachara, J. M. *Environ. Sci. Technol.* **1996**, *30*, 1618.
- (13) Mortimer, R. J. G.; Coleman, M. L.; Rae, J. E. *Sedimentology* **1997**, *44*, 759.
- (14) Frederickson, J. K.; Zachara, J. M.; Kennedy, D. W.; Dong, H.; Onstott, T. C.; Hinman, N. W.; Li, S. M. *Geochim. Cosmochim. Acta* **1998**, *62*, 3239.
- (15) Sparks, N. H. C.; Mann, S.; Bazylinski, D. A.; Lovley, D. R.; Jannasch, H. W.; Frankel, R. B. *Earth Planet. Sci. Lett.* **1990**, *98*, 14.
- (16) Warren, L. A.; Ferris, F. G. *Environ. Sci. Technol.* **1998**, *32*, 2331.
- (17) Small, T. D.; Warren, L. A.; Roden, E. E.; Ferris, F. G. *Environ. Sci. Technol.* **1999**, *33*, 4465.
- (18) Cox, J. S.; Smith, S. D.; Warren, L. A.; Ferris, F. G. *Environ. Sci. Technol.* **1999**, *33*, 4514.
- (19) Cooper, D. C.; Picardal, F.; Rivera, J.; Talbot, C. *Environ. Sci. Technol.* **2000**, *34*, 100.
- (20) Parmar, N.; Warren, L. A.; Roden, E. E.; Ferris, F. G. *Chem. Geol.* In press.
- (21) Hansma, H. G.; Hoh, J. H. *Annual Rev. Biomol. Struct.* **1994**, *23*, 115.
- (22) Bustamante, C.; Keller, D. *Physics Today* **1995**, *12*, 32.
- (23) Sokolov, I.; Firtel, M.; Henderson, G. S. J. *Vac. Sci. Technol.* **1996**, *A14*, 674.
- (24) Masini, J. C.; Godinho, E. S.; Aleixo, L. M. *Fresenius J. Anal. Chem.* **1998**, *360*, 104.
- (25) Brassard, P.; Kramer, J. R.; Collins, P. V. *Environ. Sci. Technol.* **1990**, *23*, 195.
- (26) Černík, M.; Borkovec, M.; Westall, J. C. *Environ. Sci. Technol.* **1995**, *29*, 413.
- (27) Fein, J. B.; Daughney, C. J.; Yee, N.; Davis, T. A. *Geochim. Cosmochim. Acta* **1997**, *61*, 3319.
- (28) Taylor, D. M. *Thin Solid Films* **1998**, *331*, 1.
- (29) Takano, H.; Kenseth, J. R.; Wong, S. S.; O'Brien, J. C.; Porter, M. D. *Chem. Rev.* **1999**, *99*, 2845.
- (30) Plette, A. C. C.; van Riemsdijk, W. H.; Benedetti, M. F.; van der Wal, A. J. *Colloid Interface Sci.* **1995**, *173*, 354.
- (31) Dzombak, D. A.; Morel, F. M. M. *Surface complexation modeling, hydrous ferric oxide*; Wiley-Interscience: New York, 1990.
- (32) Wilkinson, S. G. *Prog. Lipid Res.* **1996**, *35*, 283.
- (33) Siedlecki, C. A.; Marchant, R. E. *Biomaterials* **1998**, *19*, 441.
- (34) Beveridge, T. J. *J. Bacteriol.* **1999**, *181*, 4725.
- (35) Yao, X.; Jericho, M.; Pink, D.; T. Beveridge. *J. Bacteriol.* **1999**, *181*, 6865.
- (36) Zhou, L.; Srisatjaluk, R.; Justus, D. E.; Doyle, R. J. *FEMS Microbiol. Lett.* **1998**, *163*, 223.
- (37) Ferris, F. G.; Beveridge, T. J. *Can. J. Microbiol.* **1986**, *32*, 594.
- (38) Stumm, W. *Chemistry of the solid-water interface*; Wiley-Interscience: New York, 1992.
- (39) Stumm, W.; Morgan, J. J. *Aquatic Chemistry*; Wiley-Interscience: New York, 1996.

Received for review May 10, 2000. Revised manuscript received October 5, 2000. Accepted October 16, 2000.

ES001258S